Tellus (1995), 47A, 45–61
Printed in Belgium – all rights reserved

TELLUS
ISSN 0280–6495

Three-dimensional simulation of frontal rainbands and conditional symmetric instability in the Eady-wave model

By DA-LIN ZHANG*, *Department of Atmospheric and Oceanic Sciences, McGill University, Montreal, Quebec H3A 2K6, Canada*, and HAN-RU CHO, *Department of Physics, University of Toronto, Toronto, Ontario M5S 1A7, Canada*

(Manuscript received 11 August 1993; in final form 21 February 1994)

ABSTRACT

The structure and evolution of frontal rainbands in relation to conditional symmetric instability (CSI) are presented with a high-resolution, three-dimensional (3-D) simulation of an Eady wave. This work extends an earlier 2-D study of Knight and Hobbs by use of the same mesoscale model and similar initial conditions. The model simulates numerous updraft bands that correspond to the warm-sector (WSF), the surface cold frontal (SCF), the wide cold frontal (WCF) and the post-frontal (PCF) bands as observed. It is shown that the WSF band develops in a convectively near-neutral environment, while the WCF band forms under a convectively stable but slantwisely unstable condition and it interacts closely with the PCF and SCF bands. It is found that the present 3-D results conform in many respects to CSI theory and support the earlier 2-D interpretations of the rainbands. However, some differences exist, which include the development of deep and intense rainbands without downshear tilt, the deviation of the rainbands from the direction of thermal winds, strong low-level jets and intense across-frontal thermal gradients. By introducing the third spatial dimension, the model appears to show better the relationships between these rainbands and their environments, thus providing more realistic representation of the mesoscale structure and evolution of the rainbands. The importance of some physical parameters in determining the formation of various rainbands is examined. It is found that the surface friction, ice microphysics, static stability, baroclinicity and the magnitude of centrifugal forces all have important contributions to the formation, structure and dynamics of the frontal rainbands.

1. Introduction

Radar observations have revealed abundant evidence for organized mesoscale precipitating bands associated with extratropical cyclones and mesoscale convective systems (e.g., Browning and Harrold, 1969; Houze et al., 1976; Hobbs, 1978; Reuter and Yau, 1990; Zhang and Cho, 1992; Snook, 1992). These rainbands exhibit different characteristics, depending upon their environmental conditions. Some of them are convective in nature whereas others tend to form in convectively stable environments. These bands are roughly oriented along the mean wind shear with width of several tens of kilometers. A number of theoretical explanations have been proposed for the origin of the banded structures (e.g., potential instability, frontogenesis, propagating gravity waves and shearing instability), and conditional symmetric instability (CSI) has been widely accepted as a possible important mechanism for the formation of such rainbands (Bennetts and Hoskins, 1979; Emanuel, 1979; Sun, 1984; Xu, 1986; Thorpe and Rotunno, 1989).

According to CSI theory, once an air parcel becomes saturated in a region with negative moist potential vorticity (MPV) but in the absence of convective instability, it will be subject to CSI, which leads to mesoscale slantwise overturning

* Corresponding author.

with its orientation parallel to the mean vertical shear. MPV is defined here as:

$$\mathrm{MPV}=\left[\frac{\partial\theta_e}{\partial x}\left(\frac{\partial w}{\partial y}-\frac{\partial v}{\partial z}\right)+\frac{\partial\theta_e}{\partial y}\left(\frac{\partial u}{\partial z}-\frac{\partial w}{\partial x}\right)+\frac{\partial\theta_e}{\partial z}\left(\frac{\partial v}{\partial x}-\frac{\partial u}{\partial y}+f\right)\right]\Big/\rho, \quad (1)$$

where u, v and w are wind speeds (m s^{-1}) in the x, y and z directions, respectively; θ_e is equivalent potential temperature; f is the Coriolis parameter; and ρ is the density of air. MPV is conserved under inviscid and saturated adiabatic conditions, or in a two-dimensional (2-D) framework. Emanuel (1983) gave a rather simple explanation of the theory in which CSI can be viewed to represent motions resulting from a combination of buoyancy forces (through latent heat release) in the vertical and centrifugal forces in the horizontal direction. Because of the lack of high-resolution observations, verification of CSI theory has been very difficult.

With a 2-D, high-resolution, primitive equation model, Knight and Hobbs (1988), hereafter referred to as KH88, simulated the development of a cold front through shear deformation associated with the nonlinear evolution of an Eady wave. Their simulation shows clearly numerous updraft bands that are generated under a convectively stable but conditionally symmetric unstable environment. A band first forms above the surface front and intensifies in a region of negative MPV. Subsequent bands develop behind the first and intensify in the negative MPV region. The scale and behavior of the simulated updraft bands appear to correspond to observed rainbands (Hobbs, 1978) and agree with CSI theory (Emanuel, 1979; Xu, 1986). Recently, Bénard et al. (1992) have also studied the 2-D structure of frontal rainbands associated with the Eady wave; but their high-resolution, nonhydrostatic model was initialized with potentially unstable conditions near the cold frontal zone.

In this study, we extend the KH88 2-D numerical study of frontal rainbands to three spatial dimensions. Specifically, we employ the same Penn State/National Center for Atmospheric Research (PSU/NCAR) mesoscale, hydrostatic, primitive equations model (Anthes et al., 1987) but in three dimensions, as well as the same Eady wave initial conditions as those in KH88. By doing so, we seek to understand the 3-D structure of frontal rainbands and their relationships to CSI, since most of the previous studies focused on the 2-D aspects of frontal circulations and since little theoretical work has been done on 3-D CSI. As part of the understanding, we will examine, through an intercomparison between the 2-D and 3-D model results, the representativity and limitations of the 2-D findings. Another purpose of the present study is to examine the importance of some physical parameters, as expressed in eq. (1), in determining the formation and structure of various rainbands in the Eady-wave model.

In Section 2, the major features of the PSU/NCAR mesoscale model and initial conditions are briefly described. Section 3 shows the 3-D simulation of frontal rainbands and discusses the generation of 3-D structures compared to the KH88 2-D study, whereas Section 4 presents the model sensitivity of rainband generations to various physical parameters. A summary and concluding remarks are given in Section 5.

2. Model description and initial conditions

The model we used contains physical processes similar to that used by KH88, i.e., explicit calculations of cloud water and rainwater following Hsie et al. (1984), and the Blackadar medium-resolution boundary-layer parameterization (Zhang and Anthes, 1982) with the ground temperature held constant in time. The effects of condensation, evaporation and hydrostatic water loading have been included. To properly simulate the most unstable wavelength of the Eady wave (about 3000 km) in 3-D with limited computing resources, a one-way nested-grid procedure is adapted in which the coarse grid mesh (CGM) provides time-dependent tendencies for the fine grid mesh (FGM) lateral boundaries (Zhang et al., 1986). The nested-grid ratio is 1 to 3 with a FGM length of 12 km (10 km used by KH88). The (x, y, σ) dimensions for the CGM and FGM are $79\times37\times14$ and $79\times43\times14$, respectively (see Fig. 1a for the model domain). The vertical terrain-following coordinate, σ, is defined as $\sigma=(p-p_t)/(p_s-p_t)$ where p_t is the pressure at the top of the model atmosphere (308 hPa in this case) and p_s is the surface pressure. The 14 com-

putational σ layers are: 0.996, 0.986, 0.96, 0.92, 0.87, 0.81, 0.74, 0.65 and $\Delta\sigma = 0.1$ for the rest of the layers. The model is centered at 45°N with the variable Coriolis parameter. A value of $1.5 \times 10^{-4}\ s^{-2}$ is used for the static stability parameter (i.e., $N^2 = g/\theta\ \partial\theta/\partial z$), which is a little larger than that used by KH88. Specification of other constants is similar to that in KH88. It should be mentioned that both the Fritsch-Chappell (1980) and the Anthes-Kuo (Anthes et al., 1987) types of convective parameterization have been tested during initial experimental integrations, but neither of them became activated due to the absence of significant convective instability until near the end of 24-h integration.

The model is initialized with the semi-geostrophic solution to the Eady wave at $t = 60$ h (see, Hoskins and Bretherton, 1972; Keyser, 1981; Hsie et al., 1984; Reeder and Smith, 1986), with the column-integrated divergence removed. An 85% relative humidity is used to obtain initial conditions for the specific humidity. The outmost CGM lateral boundary conditions are assumed periodic in the east–west (E–W) directions while in the north–south (N–S) directions the Eady wave solution as a function of time is specified. Thus, the flow is wavelike in the E–W directions with a cold (warm) air source from the NW(SE) of the domain (see, Fig. 1a).

The E–W vertical cross section of relative flow vectors, θ_e and MPV along the central line of the CGM domain at $t = 60$ h is given in Fig. 1b. The frontal boundary is located near the center of the CGM; it translates only slightly during the model integration since the coordinate system moves eastward with a constant phase speed (i.e., $c =$

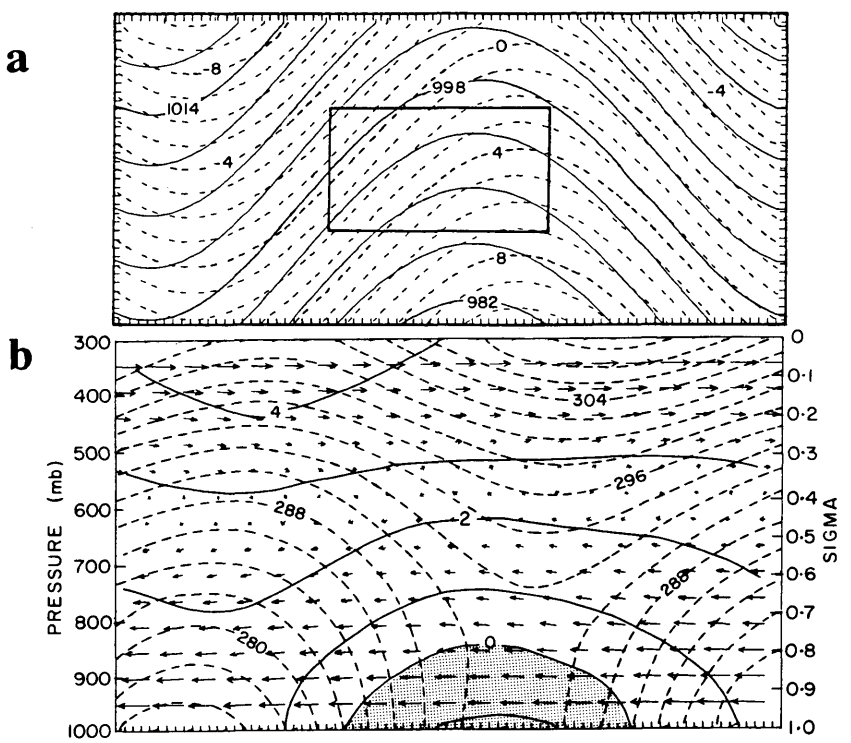

Fig. 1. Model initial conditions from the Eady-wave solution at $t = 60$ h. (a) Distribution of surface pressure (solid lines) at intervals of 4 hPa and surface temperature (dashed lines) at intervals of 1°C. The interior thick solid lines denote the nested-grid mesh interface. The intervals marked on the frame are coarse mesh grids (i.e., 36 km). (b) Vertical cross section of relative flow vectors, MPV (solid lines) at intervals of 10^{-7} K M^2 kg^{-1} s^{-1} and equivalent potential temperature (dashed lines) at intervals of 2 K along the central line of the CGM. Shadings denote a region of negative MPV.

14.35 m s^{-1}) of the analytic Eady wave (see, Keyser and Anthes, 1982). Thus, all figures will be plotted in this reference coordinate. It should be noted that due to the use of this reference coordinate, all surface fluxes except for horizontal momenta are not calculated. It is apparent from Fig. 1b that there are significant wind shears in the entire model troposphere (roughly 30 m s^{-1}/700 hPa), which are geostrophically related to the large-scale baroclinicity of the Eady wave. Vertical motion associated with the wave is rather weak initially; its maximum value is about 1 μb s^{-1} (not shown). Note the small area of slightly negative MPV (> -0.15 PV unit, 1 PV unit $= 10^{-6}$ m^2 s^{-1} K kg^{-1}) in the lowest layers which is primarily due to the presence of convectively neutral (or perhaps marginally unstable) conditions near the frontal zone. It is this weak negative MPV region that is assumed to be responsible for later formation of mesoscale rainbands. It should be mentioned that the magnitude and area coverage of negative MPV decrease northward as a result of decreases in temperature and moisture content. As will be discussed later, this N–S variation accounts primarily for the development of 3-D flow structure when condensation occurs.

Since numerous aspects of the Eady wave problem have been discussed in the literature in great detail (Hoskins and Bretherton, 1972; Keyser and Anthes, 1982; Hsie et al., 1984; Reeder and Smith, 1986; KH88; and Bénard et al., 1992), the present study will focus on the generation of various types of rainbands.

3. Numerical simulation

The PSU/NCAR 3-D model is integrated for 21 h (i.e., up to $t = 81$ h). Figs. 2a, b provide a view of the surface frontogenesis and a vertical cross section of the along-frontal winds, respectively, at $t = 81$ h from the CGM framework. When the

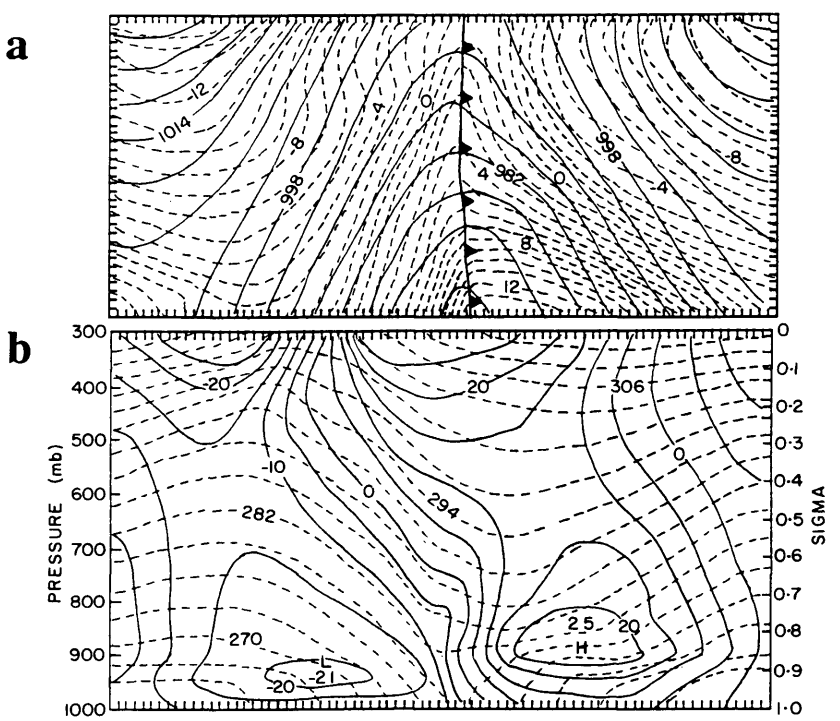

Fig. 2. The 21-h simulation of the Eady wave at $t = 81$ h. (a) As in Fig. 1a. (b) Vertical cross section of the along-frontal winds (solid lines) at intervals of 5 m s^{-1} and virtual potential temperature (dashed lines) at intervals of 3 K along the central line of the CGM.

integration proceeds, the Eady wave is gradually adjusted from the semigeostrophic mode to the primitive-equation mode through the geostrophic adjustment process. Moreover, baroclinicity increases as a result of more cold (warm) air entering the model domain through the northern (southern) boundaries. Thus, cold frontal characteristics become more apparent with time (cf., Figs. 1a, 2a). As a consequence, a southerly low- and upper-level jet couplet in the warm sector and a northerly low- and upper-level jet couplet behind the frontal zone intensify rapidly. At the end of the model integration, sharp pressure and temperature gradients develop both ahead of and behind the cold front. The intensity of the low- and upper-level jets almost doubles (cf., Fig. 1 in KH88 and Fig. 2b herein). Moreover, the wave structure is markedly distorted. To better evaluate the significance of including the third dimension, Subsections 3.1 and 3.2 present the 2-D and 3-D aspects of the frontal rainbands, respectively, whereas Subsection 3.3 compares the KH88 2-D findings with the present 3-D simulation.

3.1. Vertical cross-sectional evolution

Figs. 3a–d show vertical cross sections of vertical motion (ω, μb s^{-1}) and θ_e isopleths along the central line of the FGM from 12, 16, 18, 21 h integrations of the Eady wave at $t = 72$, 76, 78 and 81 h, respectively. Cloud boundaries and the regions of negative MPV are also superposed. By $t = 72$ h (Fig. 3a), broad regions of large-scale ascent ahead of and descent behind the front have developed, which are typical characteristics of developing cold frontal systems. As a consequence, widespread saturation occurs. The resultant latent heat release clearly helps enhance the frontal circulations. Meanwhile, 3 well-defined updraft centers have emerged from the frontal circulation, which appear to correspond to the post-frontal (PCF) band associated with the frontal return flow at the upper levels, the surface cold-frontal (SCF) band induced by the surface frictional convergence and the warm-sector frontal (WSF) band. Numerical simulations of dry and moist frontogenesis with potentially unstable stratification also produced those banded features (Keyser and Anthes, 1982; Hsie et al., 1984; Bénard et al., 1992), but with much greater magnitudes. Note that a well-mixed θ_e layer is produced across the entire wavelength due to the frictional effect. This mixing tends to generate positive MPV to compensate for the negative MPV, starting from the lowest layer (also see KH88 and Bénard et al., 1992). It also leads to a strong θ_e inversion and an increase of vertical shear near the top of the boundary layer. Thus, part of the negative MPV is dissipated in the PBL while the rest is gradually elevated and advected along the slantwise frontal zone by the frontal circulation. By this time, the area of negative MPV has been advected above the SCF band.

At $t = 76$ h, these three rainbands continue to intensify (Fig. 3b), as may be expected from frontogenesis theory. In addition, latent heating tends to narrow the scale and further strengthen the rainbands. Hence, another updraft anomaly along the frontal zone begins to emerge at the top layer of negative MPV. By 78 h, this anomaly has separated from the SCF band and become a distinct entity (Fig. 3c), as the layer of negative MPV is progressively moved upward. The width of this rainband is about 80–100 km, which agrees with the scale predicted by CSI theory (Bennetts and Ryder, 1984). The generation and behavior of this band mimic well the wide cold-frontal (WCF) band as observed by Hobbs (1978). It is evident that this band is generated under a convectively stable but symmetrically unstable condition.

While the WCF band develops in a symmetrically unstable environment, it interacts strongly with the PCF and SCF bands along the sloped frontal zone. This can be clearly seen from the associated divergence field as given in Fig. 4. At $t = 78$ h, there is a couplet of divergence above convergence associated with each rainband with stronger convergence occurring near the frontal zone. To the lower right of the WCF band, frictional convergence near the surface front forces pronounced divergence straight above to enhance convergence towards the frontal zone, while to the upper left, the PCF band causes convergence below to augment the divergence associated with the WCF band. Thus, the presence of the PCF and SCF bands is favorable for the formation of the WCF band. On the other hand, the development of the WCF band certainly affects the SCF and PCF bands through processes such as evaporative cooling and upward energy transport.

After another 3 h (i.e., $t = 81$ h), the WCF rainband not only gets further intensified, but also extends into the whole model troposphere (Fig. 3d). Clearly, this results from the positive

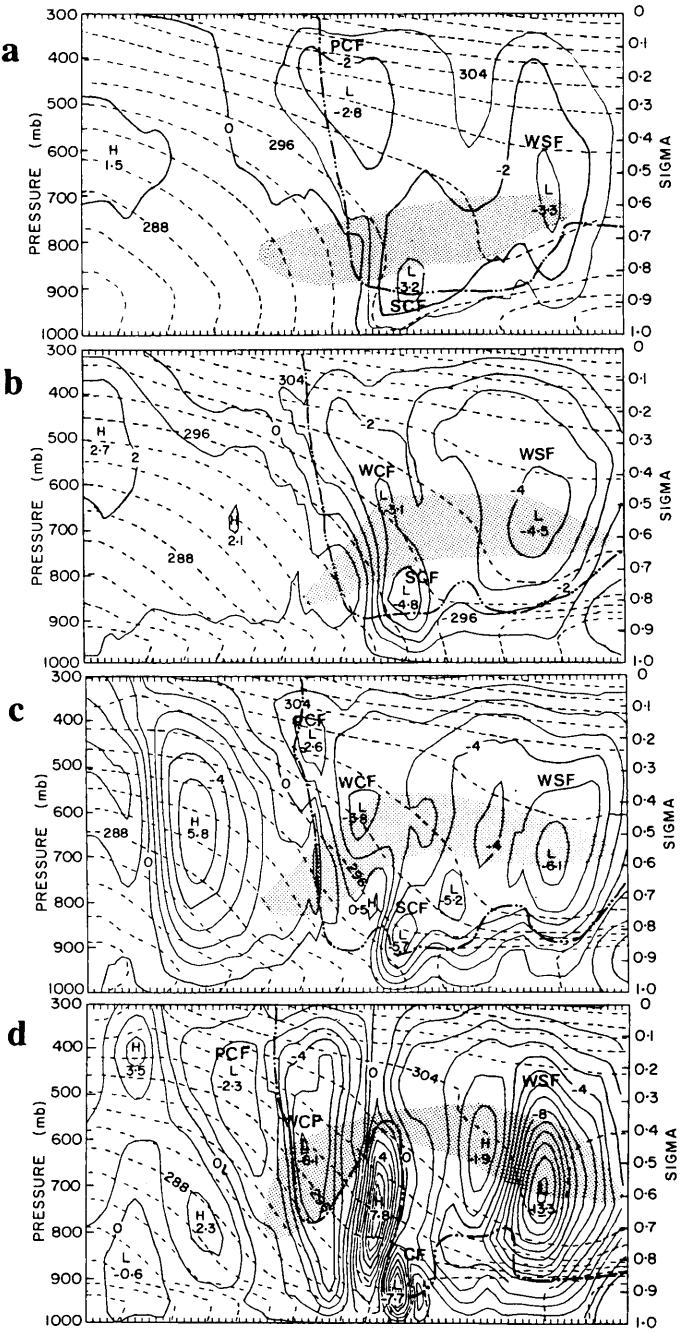

Fig. 3. Vertical cross section of vertical motion (ω, solid lines) at intervals of 1 μb s^{-1} and equivalent potential temperature (dashed lines) at intervals of 2 K along the central line of the FGM from (a) 12 h, (b) 16 h, (c) 18 h and (d) 21 h simulations of the Eady wave, corresponding to the Eady wave solution at $t = 72$, 76, 78 and 81 h, respectively. The dot-dashed line denotes cloud boundary and shadings indicate regions of negative MPV. The intervals marked on the low and upper frames are fine-mesh grids (i.e., 12 km), similarly in the rest of figures.

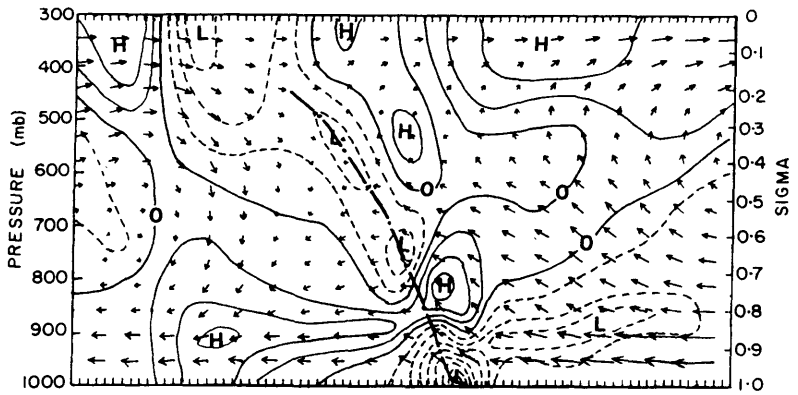

Fig. 4. Vertical cross section of relative flow vectors and convergence (dashed), divergence (solid) at intervals of 10^{-5} s^{-1} from 18 h simulation of the Eady wave at $t = 78$ h along the central line of the FGM. Thick dot-dashed lines indicate the cold frontal zone.

feedback between latent heat release and mass-moisture convergence in such a slantwisely unstable environment. During the previous five hours, the maximum intensity of the WCF band almost doubles, i.e., from -3.1 μb s^{-1} at $t = 76$ h to -6.1 μb s^{-1} at $t = 81$ h. At $t = 84$ h, its maximum upward motion within the same cross section reaches -20.5 μb s^{-1} (not shown). This corresponds to a growth rate of 6.5×10^{-5} s^{-1}, which is between the values predicted by linear CSI theory (i.e., $f = 1.0 \times 10^{-4}$ s^{-1}) and simulated in 2-D by KH88 (i.e., 1.7×10^{-5} s^{-1}).

As the WCF band amplifies rapidly, a strong downdraft, which is initiated 3 h earlier (see, Fig. 3c), appears on the downshear side of the band. This downdraft seems to be mainly forced by the compensating subsidence associated with the WCF band and enhanced somewhat by evaporative cooling. This feature also develops in a study of 2-D moist frontogenesis by Hsie et al. (1984).

As the WCF band intensifies, it tends to propagate rearward with its center roughly moving along the $\theta_e = 298$ K surface. Its horizontal displacement is about 5 to 8 m s^{-1} relative to the surface front, which is close to the mean wind in the vicinity of the WCF band (see, Fig. 5). This agrees with CSI theory and observations. As shown in Fig. 5, the front-to-rear relative winds

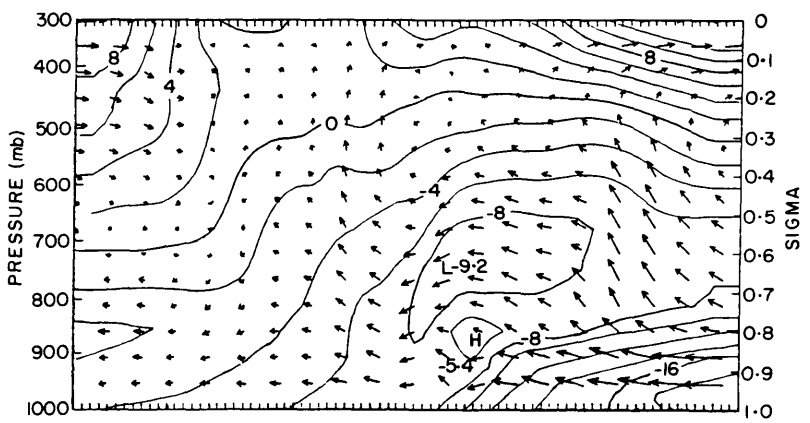

Fig. 5. Vertical cross section of relative flow vectors and relative winds normal to the front (solid lines) at intervals of 2 m s^{-1} from 21 h simulation of the Eady wave at $t = 81$ h along the central line of the FGM.

basically dominate the low- to mid-level flow ahead of the front and intensify with time. This flow structure also appears in the simulation of Reeder and Smith (1986) (see, Fig. 9a). Thus, the WCF band tends to displace toward colder air, but still with its center located within the negative MPV region. Browning and Mason (1981) too observed the rainband development in cold air behind an occluded front over the eastern North Atlantic.

Finally, it is necessary to mention that the WSF band also intensifies with time, but more rapidly than the WCF band because of the presence of the convectively less stable environment being embedded. Thus, a very strong updraft associated with the band has developed at $t = 81$ h, and thereafter it becomes more convective with time. By comparison, because of the absence of a negative MPV environment, the PCF band dissipates after its maximum intensity is reached near $t = 78$ h. At $t = 84$ h, the PCF band has been absorbed by larger-scale descent behind the front, whereas the WSF band is dominated by convective instability (not shown).

3.2. *Horizontal structure and vertical wind profiles*

Most of the features presented in the previous subsection have been discussed to a certain degree in 2-D studies of the Eady-wave problem (e.g., Hsie et al., 1984; Reeder and Smith, 1986; KH88). Since the present study is partly concerned with the 3-D structure of frontal rainbands, Figs. 6a, b show the horizontal distribution of vertical motion (ω, μb s^{-1}) at 500 and 800 hPa, respectively, superposed with the 800–500 hPa thickness isopleths from 21 h integration. These horizontal maps, together with the vertical cross sections, should provide us with necessary information on the 3-D structure of frontal rainbands except for the SCF rainband which is only confined to the boundary layer. It is evident from Fig. 6 that the updraft bands appeared in the vertical cross sections also occur three dimensionally. Of particular interest is that these bands deviate from the direction of thermal winds (about 8–10° anticyclonically), especially for the WSF band. Perhaps this is one of the most important aspects of 3-D rainbands, as compared to the 2-D counterparts. This

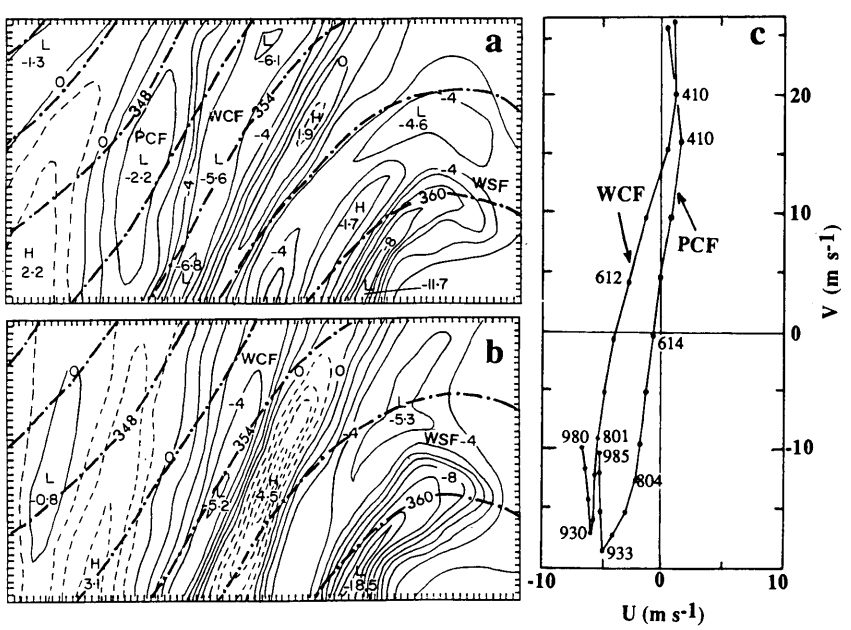

Fig. 6. Horizontal distribution of vertical motion (ω) at intervals of 1 μb s^{-1} with solid (dashed) lines indicating upward (downward) motion at (a) 500- and (b) 800-hPa from 21 h FGM simulation of the Eady wave at $t = 81$ h. Dot-dashed lines denote the thickness of the 500–800-hPa layer plotted at intervals of 3 dcm. (c) Area averaged (i.e., 36 km × 36 km) hodographs taken near the center of the WCF and PCF bands at $t = 81$ h.

result supports the findings of Jones and Thorpe (1992) in a 3-D study of CSI. They showed that such a deviation is a typical characteristic of a viscous flow; for the present study, it is a result of the use of horizontal and vertical diffusion.

Figs. 7a, b show the distribution of horizontal winds and temperature at 500 and 800 hPa, with hodographs associated with the WCF and PCF bands given in Fig. 6c. Obviously, the horizontal winds are veering (warm advection) with height ahead of and backing (cold advection) behind the frontal zone. The vertical mixing in the PBL leads to rapid deceleration of the flow in the lowest layers and an abrupt change in vertical shears near the top of the PBL. However, the wind shears aloft are roughly linear in character, and they also deviate from the orientation of the updraft bands. This is again consistent with the 3-D study of CSI by Jones and Thorpe (1992). Moreover, the bands are oriented about 15° from the surface front (cf., Figs. 2a, 6). It follows that these bands (moving with the mean wind) are not generated by gravity waves even though they appear wave-like.

3.3. *Simulation intercomparisons*

Because of numerous differences in the model design and initial conditions, rigorous intercomparisons between the KH88 2-D and the present 3-D studies are very difficult. In particular, this type of comparisons require procedures to downgrade the 3-D version of the PSU/NCAR model to a 2-D with everything, including the code of

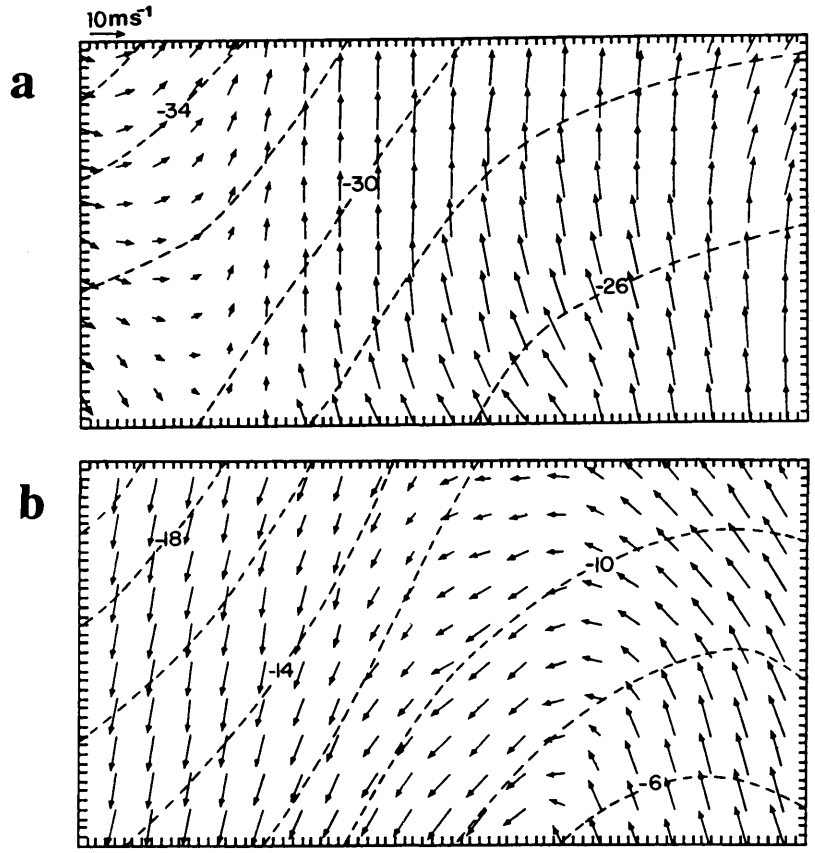

Fig. 7. Horizontal distribution of relative wind vectors and temperature at intervals of 2°C at (a) 500- and (b) 800-hPa from 21 h FGM simulation of the Eady wave at $t = 81$ h. The scale of relative wind vectors is given at the upper-left corner of the figure.

the model, being identical except for the treatment of the N–S lateral boundary conditions. Nevertheless, qualitative comparisons between these two studies are still possible, based upon the previous investigations of this type (e.g., Pielke, 1974). As has been shown, the present 3-D model reproduces well many features of the rainbands and their environmental flow conditions of the Eady wave, as compared to those simulated by Keyser and Anthes (1982), Hsie et al. (1984), Reeder and Smith (1986), Bénard et al. (1992) and KH88 with 2-D models. These include the rapid surface frontogenesis, the development of various types of updraft bands, the well-mixed PBL, the strong ageostrophic flow in the PBL, the southerly and northerly jets in the warm and cold sectors, and the elevation of negative MPV.

The differences produced between these two models are of our major concern and can be briefly described as follows. First of all, as shown in Figs. 6, 7, the rainbands and their environmental flow conditions associated with the Eady wave are three dimensional in character, such as the curved flow and the deviation of the rainbands from thermal winds. These 3-D characters can be attributed primarily to the northward decrease of moisture content associated with the initial moist Eady wave. Thus, condensation would tend to occur earlier in the warm sector in the south and then extend northward gradually. This is evidenced by a general northeastward reduction of vertical motion (see, Fig. 6), although there appear to be some slight numerical problems near the northern and southern boundaries. Moreover, the use of numerical diffusivity allows constant angular momentum surfaces to cross over; thus, it tends to further destroy the 2-D structure of the initial Eady-wave solution. In particular, the WSF band would not appear if an E–W cross section is taken to the north of the Eady wave (see, Fig. 6). Note that Jones and Thorpe (1992) also presented the development of 3-D circulation structures from 2-D initial conditions even in the absence of diabatic heating. Second, updrafts in KH88 tend to lean downshear and propagate towards the warm sector. The downshear tilt is a well-known problem in 2-D simulations with deep sheared environments (e.g., Seitter and Kuo, 1983); it may have also partially helped generate the multiple WCF bands in KH88 (see, Fig. 8) because a deeper portion of the tilted updrafts would be embedded in a layer of negative MPV. Of course, other differences in the model parameters may too have contributed to the generation of the multiple bands, such as the grid size and static stability. Third, the 2-D model fails to produce the deep and strong growth of the rainbands in the presence of negative MPV (cf., Fig. 8 in KH88 and Fig. 3 herein). At the end of their 27 h integration (i.e., $t = 87$ h), the maximum intensity of the WCF bands is only about 6 cm s^{-1} (see, Fig. 8e in KH88). The development of the relatively weak vertical motion may be related to the unrealistic representation of divergence, and vortex stretching and tilting in 2-D models when environmental wind shears are strong and longitudinal lateral

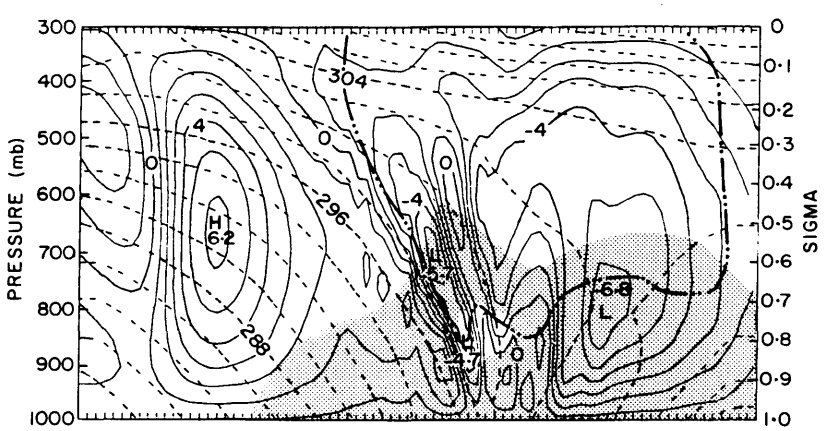

Fig. 8. As in Fig. 3c but for Exp. FRC (no surface friction).

boundary conditions are specified. The downshear tilt of updrafts may be also a consequence of this effect. That is, the downshear tilt tends to suppress deep vertical circulations, based on the previous cloud modeling studies (Thorpe et al., 1982; Seitter and Kuo, 1983). Likewise, the low-level along-frontal jets in the 2-D model are about 5 m s^{-1} weaker than that in the 3-D model, even as compared to the present CGM simulation (cf., Fig. 17 in KH88 and Fig. 2b herein). This indicates the development of relatively weak across-frontal thermal gradients and the transport of less amount of high-θ_e air or negative MPV along the front for the development of rainbands. Thus, it appears that although a 2-D model can yield most of the basic features associated with the frontal rainbands, a full 3-D model is required to obtain more realistic solutions. Recent theoretical and observational studies of frontal rainbands by Jones and Thorpe (1992) and Roux et al. (1993) also point to the same conclusion.

4. Sensitivity experiments

To help gain insight into the significance of various physical parameters in the development of frontal rainbands, a series of sensitivity experiments are conducted with the simulation described in Section 3 as a control run (Exp. CTL). Each experimental simulation has conditions identical to Exp. CTL except for the treatment of a particular parameter. Physical parameters to be examined here include friction (FRC) in the PBL, ice microphysics (ICE), static stability (STB), baroclinicity (BCN) and inertial forces through variation of latitudes (LAT). Details of these simulations are discussed below.

4.1. Effect of friction

In Exp. CTL, the Blackadar PBL parameterization scheme (Zhang and Anthes, 1982) provides the vertical mixing mechanism whereby the lowest layer acts as sinks of heat, moisture and momentum. Therefore, turbulent mixing can create a well-mixed PBL ahead of and behind the surface front (Fig. 3) even with the ground temperature fixed in time in this study. In Exp. FRC, the friction is eliminated by not allowing the momentum flux to cross the surface layer, in addition to the absence of surface heat and moisture fluxes. Without the surface fluxes, no vertical mixing can possibly take place. Thus, the slope and distribution of θ_e surfaces in the lower levels change little during the model integration (Fig. 8), as expected. Furthermore, the capped inversion fails to develop (cf., Figs. 3c, 8), and maximum winds remain in the lowest layer.

Perhaps one of the most relevant results to Exp. FRC is that unlike Exp. CTL, negative MPV remains in the PBL and its volume expands continuously from the surface to higher levels due partly to the response to the frontal circulation and partly to precipitation fallouts and the numerical diffusion that is included in the model for controlling numerical aliasing. Of course, the average magnitude of negative MPV decreases slowly with time due to the latter two factors. A comparison of Figs. 3c, 8 shows that the surface friction is clearly a source of MPV. This is consistent with a recent study by Cooper et al. (1992), who show that the frictional effects in strong baroclinic zones act to generate a local maximum in PV. (Note, though, that the PBL could be a sink of MPV when surface heat and moisture fluxes overpower the frictional effects.) Most of positive MPV is generated through its vertical component as a result of the development of a θ_e inversion and an increase of vertical shear.

Because of the neglect of friction, the model produces relatively weak upward motion associated with the SCF band, which agrees with the findings of Keyser and Anthes (1982). Of particular significance is that only a single slantwise cell develops along the tilted frontal zone at $t = 78$ h (cf., Figs. 3d, 8). One can imagine from Fig. 4 why only one cell could be generated when the friction-induced divergence is markedly reduced. This will lead to the distribution of a deep convergence zone along the frontal surface. The one-cell generation also explains why many theoretical studies of CSI, in which surface mixing processes are not included, often show a single cell of slantwise convection. The WCF band does not separate from the cell until near $t = 84$ h when its intensity exceeds $-20\ \mu b\ s^{-1}$ (not shown). This simulation suggests that the surface friction can have a significant effect on the flow structure not only in the PBL but also 200–300 hPa above the PBL. Similarly, horizontal diffusion must have also contributed to the dissipation of negative MPV. One of the examples can be seen from a

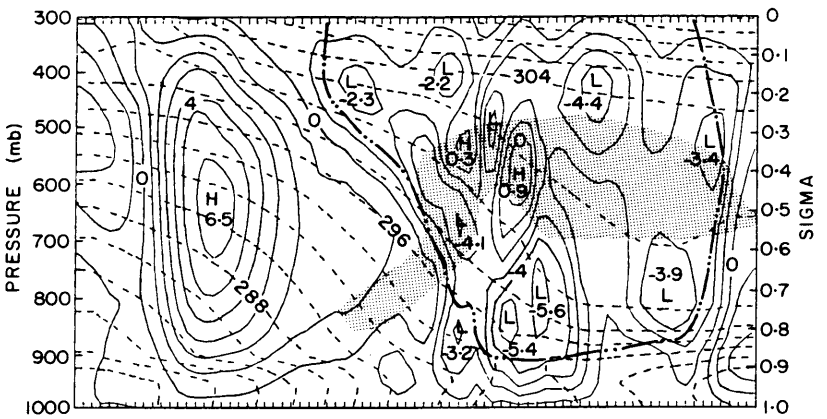

Fig. 9. As in Fig. 3c but for Exp. ICE (with ice microphysics).

sharp decrease in the thickness of a negative MPV layer near the eastern FGM boundary where stronger horizontal diffusion is imposed to reduce possible numerical noises along the interface (see, Zhang et al., 1986; Anthes et al., 1987). The reader is referred to Keyser and Anthes (1982) for more detailed discussion of the effects of the surface friction on the surface cold frontogenesis.

4.2. Effect of ice microphysics

There has been considerable observational evidence that ice microphysics plays an important part, through the "seeder-feeder" process, in the formation of frontal rainbands and the enhancement of associated precipitation (Browning and Harrold, 1969; Hobbs et al., 1980; Matejka et al., 1980). Thus, it is desirable to test this aspect by turning on the explicit calculations of cloud ice and snow in the model (see, Zhang, 1989; Dudhia, 1989). The ice microphysics package used here contains processes of depositional growth of cloud ice/snow and accretion of ice crystals by snow, in addition to the ice-snow autoconversion, freezing and melting effects.

With the ice microphysics included, the gross distribution of the rainbands resembles closely that in Exp. CTL (Fig. 9), although their magnitudes differ. One of the most striking features is that the inclusion of ice microphysics produces more mesoscale structures that also tend to be more 3-D in character, especially at the middle to upper levels. This characteristic has also been noted by Lord et al. (1984) in a simulation of a tropical cyclone when an ice microphysics package similar to the present one was incorporated. It is evident from Fig. 9 that the sublimative/depositional latent heat is responsible for several updraft cells in the upper levels, which in turn tends to enhance the ice/snow production, thereby providing a positive feedback mechanism for rainfall development. As snow particles fall through the cells below, they affect the dynamic as well as thermodynamic fields of the lower-level cells through continued deposition, accretion, melting, evaporation and water loading. Thus, the updrafts at the lower levels are relatively weak, especially in the warm sector, as compared to Exp. CTL (cf., Figs. 9, 3c).

Fig. 10 compares the time evolution of the FGM domain-integrated hourly rainfall rate between

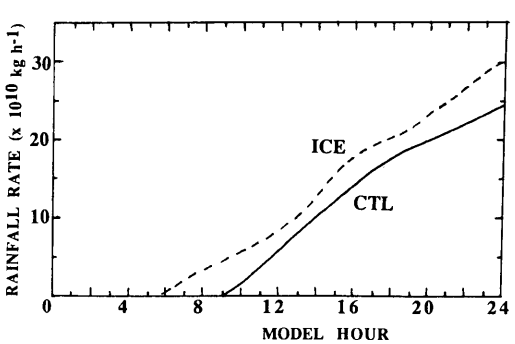

Fig. 10. The FGM-integrated hourly rainfall rate (10^{10} kg h^{-1}) as a function of the model hour for Exp. CTL (solid line) and ICE (dashed lines).

Exps. CTL and ICE. With the inclusion of ice microphysics, precipitation begins to develop about three hours earlier and the rainfall rate is enhanced by a factor of 20–30% throughout the model integration. These results are consistent with a real-data numerical case study of mesoscale convective systems by Zhang (1989), and observational studies by Herzegh and Hobbs (1980) and Houze et al. (1981) in which about 20–35% of total precipitation originates from the "seeder" region.

4.3. *Effect of static stability*

We have demonstrated that rainbands can (e.g., WCF bands) form in a convectively stable but symmetrically unstable environment. One may wonder whether or not the rainbands could develop when the initial conditions are more convectively stable such that negative MPV (i.e., CSI) is no longer present (see eq. (1)). This is done here by setting $N^2 = 1.8 \times 10^{-4}\ s^{-2}$ in the initial conditions (Exp. STB). With the greater static and symmetric stability, the centrifugal forces tend to dominate the buoyancy forces in the generation of favorable upward motion along the frontal zone. Thus, the WCF and PCF bands fail to form even at the end of 24 h integration (see, Fig. 11). Meanwhile, the model produces relatively weak frontal circulations, and cold frontogenesis is significantly suppressed. The results reveal that the formation of the WCF and PCF rainbands may depend upon the extent of cold frontogenesis, since baroclinicity can provide favorable forcing for the initiation of convection along the cold front (Hoskins et al., 1984; Cho and Chan, 1987).

When the static stability is significantly reduced (i.e., $N^2 = 1.2 \times 10^{-4}\ s^{-2}$), the model is able to produce several bands; but they are similar to that in Hsie et al. (1984) and Bénard et al. (1992), namely, convective modes dominate frontal circulations as well as rainfall production, particularly in the warm sector of the frontal system. Thus, they are not shown here because upright convection is not of our concern for the present study.

4.4. *Effect of baroclinicity*

It is evident from eq. (1) that baroclinicity is also an important factor in determining the magnitude of MPV or the degree of CSI. Thus, in this experimental simulation, the magnitude of the N–S temperature gradient is reduced from -1 to -0.75°C/100 km (Exp. BCN). Evidently, this will reduce the coverage of negative MPV at the model initial time. In fact, with this magnitude, the layer of negative MPV almost disappears from the initial conditions. As a result, the model fails to reproduce the control-simulated bands along the frontal zone (Fig. 12). Moreover, the model is unable to simulate the SCF band even at $t = 84$ h, and the intensity of frontal circulations is similar to that in Exp. STB. This indicates that a decrease in baroclinicity is equivalent to an increase in static stability in affecting the formation of various bands.

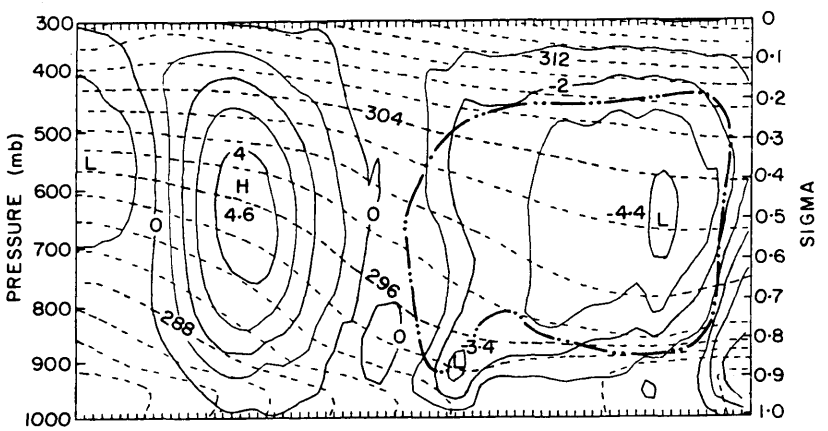

Fig. 11. As in Fig. 3c but for Exp. STB (increased static stability) from 24 h FGM simulation of the Eady wave at $t = 84$ h.

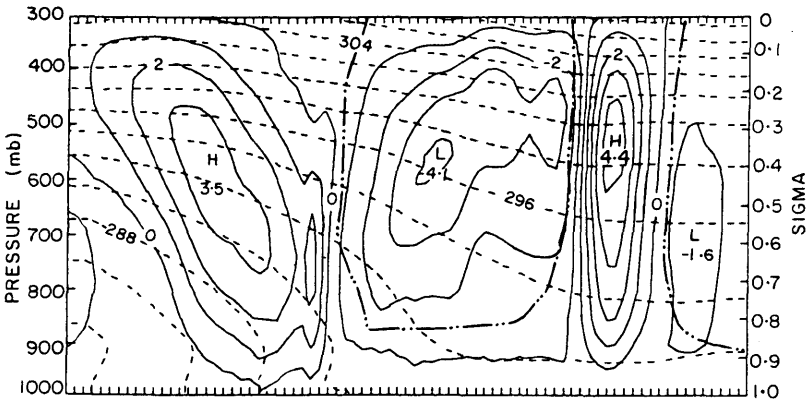

Fig. 12. As in Fig. 3c but for Exp. BCN (decreased baroclinity) from 24 h FGM simulation of the Eady wave at $t = 84$ h.

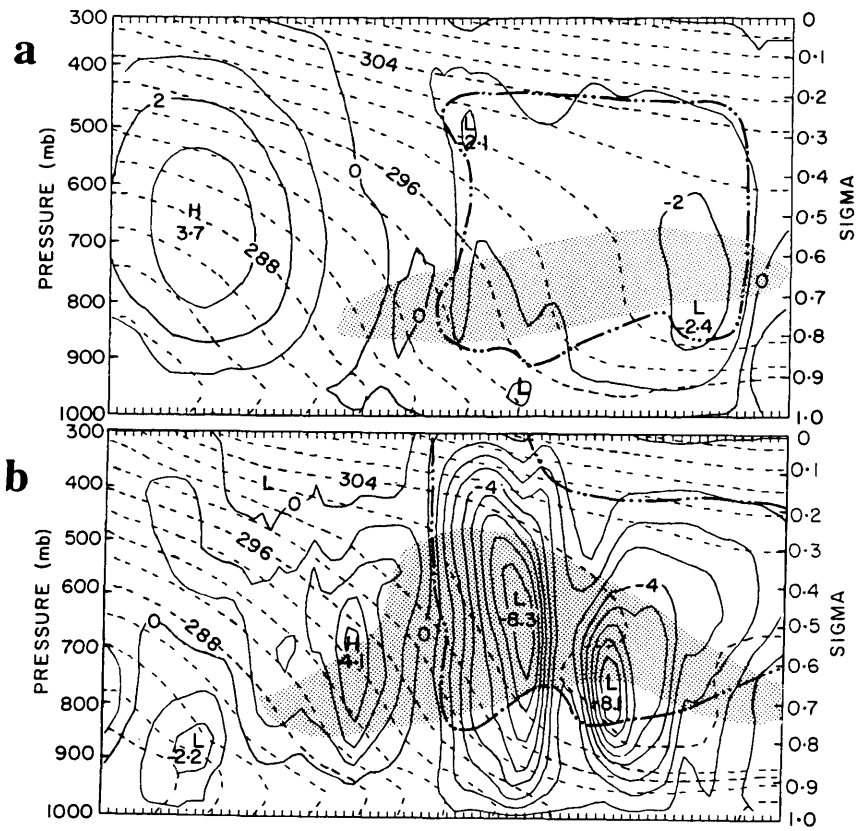

Fig. 13. As in Fig. 3c but for Exp. LAT (increased latitude) from (a) 18 h and (b) 24 h FGM simulations of the Eady wave at $t = 78$ and 84 h, respectively.

Conversely, when the N–S temperature gradient increases to $-1.25°C/100$ km, the coverage of MPV becomes deeper and wider. Thus, all frontal bands amplify rapidly during the first 12 h of the integration, which is similar to the case of decreasing the static stability. Their intensities at $t = 72$ h are even much stronger than those in the control simulation at $t = 84$ h (not shown). Thus, the presence of negative MPV at $t = 60$ h is essential in determining whether or not the WCF band could develop under a baroclinic atmosphere. This aspect can be further demonstrated in the next experimental simulation.

4.5. Effect of latitude

Since the slantwise circulation is a resultant of the buoyancy and centrifugal forces, it is of interest to investigate the behavior of rainbands when stronger centrifugal forces are imposed (Exp. LAT). This can be achieved by moving the center of the Eady wave to a higher latitude (i.e., 75° N in this case). It is evident from eq. (1) and Fig. 1b that this procedure will enhance somewhat the negative MPV areas where marginally convective instability is present near the surface frontal zone, and the positive MPV areas elsewhere. Nevertheless, enhanced negative MPV does not seem to have a positive impact on the formation of frontal rainbands (Fig. 13). Even at $t = 78$ h (Fig. 13a), the banded structure has yet become evident although upward motion has become dominated ahead of the frontal zone (saturation implies upward motion). The WCF band does not appear as a distinct entity until $t = 81$ h (not shown) and become well developed near $t = 84$ h (Fig. 13b). As compared to Exps. STB and BCN in which the WCF band is not generated owing to the absence of negative MPV, an increase in the centrifugal forces in the present case is able to reproduce the development of various bands, but at a later time. The result further indicates the importance of having negative MPV in the initial conditions of the Eady wave solution. Thus, one may conjecture that the effect of increasing centrifugal forces tends to enhance the horizontal component of the slantwise circulation and delay the occurrence of slantwise convection until the required buoyancy forces are strong enough such that the resultant vertical circulation vectors tilt at greater angles toward the vertical relative to the slope of θ_e isopleths.

In contrast, when the Eady wave is centered along a lower latitude (i.e., at 15° N), upright convection quickly dominates the frontal circulation due to the decrease of centrifugal forces. The use of unrealistic baroclinicity (i.e., $1°C/100$ km) for a low-latitude environment is also part of the reason for the earlier generation of upright convection during the initial geostrophic adjustment of the Eady wave.

5. Summary and conclusions

In this study, a 3-D simulation of frontal rainbands associated with the Eady wave has been performed using the PSU/NCAR mesoscale hydrostatic model. As in the KH88 2-D study, the model simulates numerous updraft bands that correspond to the warm-sector (WSF), the surface cold frontal (SCF), the wide cold frontal (WCF) and the post-frontal (PCF) bands as observed. It has been shown that the WCF band tends to develop in an elevated region of negative MPV along the frontal zone. The band has a width of 80–100 km with its orientation deviated from the direction of thermal winds. It moves rearward with mean winds, and intensifies rapidly with time. The WCF band appears to interact closely with the SCF and PCF bands along the sloped frontal zone. The results suggest that realistic simulations of the frontal rainbands do not require use of non-hydrostatic models, since they develop in convectively stable conditions.

Although the present results support many of the earlier 2-D interpretations of rainbands by KH88 and other studies of the Eady wave problem, there are some major differences introduced primarily by including the third spatial dimension. They include the development of deep and intense frontal rainbands without significant downshear tilt, strong low-level jets, the northeastward reduction of vertical motion in curved flows and across-frontal thermal gradients. More importantly, the orientation of 3-D raindbands tends to deviate from the direction of thermal winds by 8–10°. Therefore, with the present 3-D configuration, we are able to better demonstrate the relationships between frontal rainbands and their environmental conditions. We may state that a full 3-D model is required to obtain more realistic simulations of the frontal rainbands.

Inclusions of the PBL, diffusivity, condensation, ice microphysics and weak static stability conditions tend to cause the frontal circulations and CSI more 3-D in character.

A series of sensitivity experiments are carried out to gain insight into the importance of some physical parameters in determining the generation of the frontal rainbands. The results clearly reveal that the frictional effects in the PBL, ice microphysics, static stability, baroclinicity and the magnitude of inertial forces all play significant roles in the formation, structure and dynamics of the frontal rainbands. Without the surface fluxes of heat, moisture and momentum, the negative MPV initially located in the lower layers persists and expands vertically in response to frontal circulations. Only a single slantwise cell could develop along the frontal zone. Inclusion of ice microphysics gives rise to more mesoscale structures, the earlier triggering of grid-box saturation and the enhancement of precipitation. Thus, this full physics simulation yields more realistic representation of the frontal rainbands in nature. An increase in static stability is equivalent to a decrease in baroclinicity in creating an unfavorable environment for the formation of the WCF band. With an increase in the centrifugal forces, the model tends to generate a weaker WCF band and delay the appearance of the associated characteristics. The results suggest that the presence of negative MPV in the initial conditions, even it is small, is instrumental in determining the subsequent development of various rainbands. The results also suggest that slantwise convective mode tends to dominate the type of precipitation during the cold season and in higher latitudes, whereas under the warm season, weak-gradient environments or in lower latitudes, upright convective mode would prevail.

It should be noted, however, that the above conclusions are drawn from a highly idealized initial conditions and very difficult to be verified against observations, since it requires dynamically consistent, high spatial and temporal resolution observations. In addition, the small values of negative MPV, required to trigger slantwise convection, may be within the error range of measurements. Nevertheless, recent studies by Emanuel (1985), Thorpe and Emanuel (1985), Reuter and Yau (1990) and others have shown the development of slantwise convection in the presence of small moist symmetric stability, but only in a 2-D framework. Thus, much needed research should be carried out in the future to clarify the relationship between the rainband formation and CSI in a 3-D framework.

6. Acknowledgments

We are very grateful to Dave Knight for his stimulating discussions and to two anonymous reviewers for their helpful comments. The computations were performed at the University of Toronto's CRAY X-MP and NCAR's Y-MP. This research is supported by Natural Sciences and Engineering Research Council and Atmospheric Environmental Service of Canada.

REFERENCES

Anthes, R. A., Hsie, E.-Y. and Kuo, Y.-H. 1987. *Description of the Penn State/NCAR mesoscale model version 4 (MM4)*. NCAR Tech. Note, NCAR/TN-282, 66 pp.

Bénard, P., Lafore, J.-P. and Redelsperger, J.-L. 1992. Nonhydrostatic simulation of frontogenesis in a moist atmosphere. Part II: Moist potential vorticity budget and wide rainbands. *J. Atmos. Sci.* **49**, 2218–2235.

Bennetts, D. A. and Hoskins, B. J. 1979. Conditional symmetric instability, a possible explanation for frontal rainbands. *Quart. J. Roy. Meteor. Soc.* **105**, 945–962.

Bennetts, D. A. and Ryder, P. 1984. A study of mesoscale convective bands behind cold fronts. Part I: Mesoscale organization. *Quart. J. Roy. Meteor. Soc.* **110**, 121–145.

Browning, K. A. and Harrold, T. W. 1969. Air motion and precipitation growth in a wave depression. *Q. J. Roy. Meteor. Soc.* **95**, 288–309.

Browning, K. A. and Mason, B. J. 1981. Air motion and precipitation growth in frontal systems. *Pure and Appl. Geophys.* **119**, 577–593.

Cho, H.-R. and Chan, D. S. 1987. Mesoscale atmospheric dynamics and modeling of rainfall fields. *J. Geophys. Res.* **92**, 9687–9692.

Cooper, I. M., Thorpe, A. J. and Bishop, C. H. 1992. The role of diffusive effects on potential vorticity at fronts. *Quart. J. Roy. Meteor. Soc.* **118**, 629–647.

Dudhia, J. 1989. Numerical study of convection observed during the Winter Monsoon Experiment using a mesoscale two-dimensional model. *J. Atmos. Sci.* **46**, 3077–3107.

Emanuel, K. A. 1979. Inertial instability and mesoscale convective systems. Part I: Linear theory of inertial instability in rotating viscous fluid. *J. Atmos. Sci.* **36**, 2425–2449.

Emanuel, K. A. 1983. On assessing local conditional symmetric instability from atmospheric soundings. *Mon. Wea. Rev.* **111**, 2016–2033.

Emanuel, K. A. 1985. Frontal circulations in the presence of small moist symmetric stability. *J. Atmos. Sci.* **42**, 1062–1071.

Fritsch, J. M. and Chappell, C. F. 1980. Numerical prediction of convectively driven mesoscale pressure systems. Part I: Convective parameterization. *J. Atmos. Sci.* **37**, 1722–1733.

Herzegh, P. H. and Hobbs, P. V. 1980. The mesoscale and microscale structure and organization of clouds and precipitation in midlatitude cyclones (II). Warm-frontal clouds. *J. Atmos. Sci.* **37**, 597–611.

Hobbs, P. V. 1978. Organization and structure of clouds and precipitation on the mesoscale and microscale in cyclonic storms. *Rev. Geophys. Space Phys.* **16**, 741–755.

Hobbs, P. V., Matejka, T. J., Herzegh, P. H., Locatelli, J. D. and Houze, R. A., Jr. 1980. The mesoscale and microscale structure and organization of clouds and precipitation in midlatitude cyclones. I: A case study of a cold front. *J. Atmos. Sci.* **37**, 568–596.

Hoskins, B. J. and Bretherton, F. 1972. Atmospheric frontogenesis models: Mathematical formulation and solution. *J. Atmos. Sci.* **29**, 11–37.

Hoskins, B. J., Neto, E. C. and Cho, H.-R. 1984. The formation of multiple fronts. *Quart. J. R. Meteor. Soc.* **110**, 881–896.

Houze, R. A., Jr., Hobbs, P. V., Biswas, K. R. and Davis, W. M. 1976. Mesoscale rainbands in extratropical cyclones. *Mon. Wea. Rev.* **104**, 868–878.

Houze, R. A., Jr., Rutledge, S. A., Matejka, T. J. and Hobbs, P. V. 1981. The mesoscale and microscale structure and organization of clouds and precipitation in midlatitude cyclones. III: Air motion and precipitation growth in a warm-frontal rainband. *J. Atmos. Sci.* **38**, 639–649.

Hsie, E.-Y., Anthes, R. A. and Keyser, D. 1984. Numerical simulation of frontogenesis in a moist atmosphere. *J. Atmos. Sci.* **41**, 2581–2594.

Jones, S. C. and Thorpe, A. J. 1992. The three-dimensional nature of "symmetric" instability. *Q. J. R. Meteor. Soc.* **118**, 227–258.

Keyser, D. 1981. *Frontogenesis in the planetary boundary layer of an amplifying, two-dimensional baroclinic wave.* PhD thesis, The Penn. State University, 285 pp.

Keyser, D. and Anthes, R. A. 1982. The influence of planetary boundary layer physics on frontal structure in the Hoskins–Bretherton horizontal shear model. *J. Atmos. Sci.* **39**, 1783–1802.

Knight, D. J. and Hobbs, P. V. 1988. The mesoscale and microscale structure and organization of clouds and precipitation in midlatitude cyclones. Part XV: A numerical modeling study of frontogenesis and cold-frontal rainbands. *J. Atmos. Sci.* **45**, 915–930.

Lord, S. J., Willoughby, H. E. and Piotrowicz, J. M. 1984. Role of a parameterized ice-phase microphysics in an axisymmetric, nonhydrostatic tropical cyclone model. *J. Atmos. Sci.* **41**, 2836–2848.

Matejka, T. J., Houze, R. A., Jr. and Hobbs, P. V. 1980. Microphysics and dynamics of clouds associated with mesoscale rainbands in extratropical cyclones. *Q. J. Roy. Meteor.* **106**, 29–56.

Pielke, R. A. 1974. A comparison of three-dimensional and two-dimensional numerical predictions of sea breezes. *J. Atmos. Sci.* **31**, 1577–1585.

Reeder, M. J. and Smith, R. K. 1986. A comparison between frontogenesis in the two-dimensional Eady model of baroclinic instability and summertime cold fronts in the Australian region. *Quart. J. Roy. Meteor. Soc.* **112**, 293–313.

Reuter, G. W. and Yau, M. K. 1990. Observations of slantwise convective instability in winter cyclones. *Mon. Wea. Rev.* **118**, 447–458.

Roux, F., Marécal, V. and Hauser, D. 1993. The 12/13 January 1988 narrow cold-frontal rainband observed during MFDP/FRONTS 87. Part I: Kinematics and thermodynamics. *J. Atmos. Sci.* **50**, 951–974.

Seitter, K. L. and Kuo, H.-L. 1983. The dynamical structure of squall-line type thunderstorms. *J. Atmos. Sci.* **40**, 2831–2854.

Snook, J. S. 1992. Current techniques for real-time evaluation of conditional symmetric instability. *Weather & Forecasting* **7**, 430–439.

Sun, W.-Y. 1984. Rainbands and symmetric instability. *J. Atmos. Sci.* **41**, 3412–3426.

Thorpe, A. J. and Emanuel, K. A. 1985. Frontogenesis in the presence of small stability to slantwise convection. *J. Atmos. Sci.* **42**, 1809–1824.

Thorpe, A. J. and Rotunno, R. 1989. Nonlinear aspects of symmetric instability. *J. Atmos. Sci.* **46**, 1285–1299.

Thorpe, A. J., Miller, M. J. and Moncrieff, M. W. 1982. Two-dimensional convection in nonconstant shear: a model of midlatitude squall line. *Q. J. Roy. Meteor. Soc.* **108**, 739–762.

Xu, Q. 1986. Conditional symmetric instability and mesoscale rainbands. *Quart. J. Roy. Meteor. Soc.* **112**, 315–334.

Zhang, D.-L. 1989. The effect of parameterized ice microphysics on the simulation of vortex circulation with a mesoscale hydrostatic model. *Tellus* **41A**, 132–147.

Zhang, D.-L. and Anthes, R. A. 1982. A high-resolution model of the planetary boundary layer, sensitivity tests and comparisons with SESAME-79 data. *J. Appl. Meteor.* **21**, 1594–1609.

Zhang, D.-L., Chang, H.-R., Seaman, N. L., Warner, T. T. and Fritsch, J. M. 1986. A two-way interactive nesting procedure with variable terrain resolution. *Mon. Wea. Rev.* **114**, 1330–1339.

Zhang, D.-L. and Cho, H.-R. 1992. The development of negative moist potential vorticity in the stratiform region of a simulated squall line. *Mon. Wea. Rev.* **120**, 1322–1341.